Nanoscale

PAPER

View Article Online
View Journal

Cite this: DOI: 10.1039/d0nr02991b

Ultrathin Bi_2O_2S nanosheet near-infrared photodetectors†

Basant Chitara,[a] Tej B. Limbu,[a] Jason D. Orlando,[a] Yongan Tang[b] and Fei Yan *[a]

Recently, a zipper two-dimensional (2D) material Bi_2O_2Se belonging to the layered bismuth oxychalcogenide (Bi_2O_2X: X = S, Se, Te) family, has emerged as an alternate candidate to van der Waals 2D materials for high-performance electronic and optoelectronic applications. This hints towards exploring the other members of the Bi_2O_2X family for their true potential and bismuth oxysulfide (Bi_2O_2S) could be the next member for such applications. Here, we demonstrate for the first time, the scalable room-temperature chemical synthesis and near-infrared (NIR) photodetection of ultrathin Bi_2O_2S nanosheets. The thickness of the freestanding nanosheets was around 2–3 nm with a lateral dimension of ~80–100 nm. A solution-processed NIR photodetector was fabricated from ultrathin Bi_2O_2S nanosheets. The photodetector showed high performance, under 785 nm laser illumination, with a photoresponsivity of 4 A W^{-1}, an external quantum efficiency of 630%, and a normalized photocurrent-to-dark-current ratio of 1.3 × 10^{10} per watt with a fast response time of 100 ms. Taken together, the findings suggest that Bi_2O_2S nanosheets could be a promising alternative 2D material for next-generation large-area flexible electronic and optoelectronic devices.

Received 15th April 2020,
Accepted 7th July 2020

DOI: 10.1039/d0nr02991b

rsc.li/nanoscale

Introduction

Infrared (IR) photodetectors find a myriad of applications in thermal imaging, biomedical imaging, night vision, information communication, military *etc.*[1–3] The specific wavelength of detection is achieved by choosing materials with desirable band gaps. Silicon[4] and germanium[5] have been commercialized for near-infrared (NIR) photodetection for a long time. However, these materials cannot be used in bendable and flexible optoelectronics.[6] Therefore, there is a continuous interest for finding new materials with high mechanical strength, tunable bandgap, high absorption and relative ease of availability to be processed as flexible substrates for IR photodetection. 2D materials offer excellent electronic[1,7–9] and mechanical properties,[10–12] thus fulfilling the aforementioned prerequisites for large-area and low-cost IR photodetection applications. Following this, several IR photodetectors have been fabricated from graphene,[1] transition metal dichalcogenides (TMDs),[3,13] black phosphorus (BP),[14–19] and MXenes.[20] However, graphene suffers from the absence of bandgap and low light absorption[1,17] and TMDs, BP, and MXenes require complex encapsulation[18,19] and/or functionalization,[20] which prompts further exploration of alternative 2D materials for such applications.

Recently, a new 2D air-stable bismuth oxyselenide[21–25] (Bi_2O_2Se) owing to its extremely high carrier mobility (>20 000 cm^2 V^{-1} s^{-1} at 2 K), low effective mass ($0.14m_0$) and bandgap tunability has revolutionized the research in the bismuth oxychalcogenide (Bi_2O_2X: X = S, Se, Te) family, which is complementary to van der Waals (vdW) 2D materials for high-performance electronic and optoelectronic applications. Bi_2O_2X have been extensively studied for their thermoelectric properties and some research has been devoted to their electronic[21] and optoelectronic properties.[24,26–29] However, in all of the aforementioned studies highlighting Bi_2O_2Se, it has been obtained by synthesis techniques such as chemical vapor deposition (CVD), physical vapor deposition and crystal growth methods requiring high temperature. Moreover, Bi_2O_2Se contains selenium which is highly toxic in nature.[30] Thus, it would be interesting to explore Bi_2O_2S, another member belonging to the same family which is selenium-free and offers the possibility of room-temperature synthesis. Bi_2O_2S has an orthorhombic crystal structure with a space group of *Pnnm*.[31] It exhibits a bandgap of 1.5 eV, and possesses efficient charge dissociation, high charge carrier transport and long carrier lifetime.[32–34] The one key aspect of these layered 2D materials making them different from vdW 2D materials is the presence of a weak interlayer interaction in contrast to vdW interaction. The loosely packed structure of Bi_2O_2S can be

[a]Department of Chemistry and Biochemistry, North Carolina Central University, Durham, NC 27707, USA. E-mail: chitara.basant@gmail.com, fyan@nccu.edu
[b]Department of Mathematics and Physics, North Carolina Central University, Durham, NC 27707, USA

†Electronic supplementary information (ESI) available. See DOI: 10.1039/d0nr02991b

exploited in photocatalytic and photovoltaic applications.[35,36] Moreover, Bi_2O_2S has been predicted to exhibit ferroelectricity/ferroelasticity.[37] Therefore, Bi_2O_2S provides a unique combination of semiconducting properties with ferroelectric/ferroelastic properties for next-generation electronic and optoelectronic devices. In the present investigation, ultrathin free-standing Bi_2O_2S nanosheets have been synthesized at room temperature in contrast to hydrothermal and chemical bath deposition reported in the literature.[31–33,35,36] While both methods have the ability to grow large and good quality crystals, the hydrothermal synthesis method suffers from certain drawbacks such as needing expensive autoclaves and high temperature and the difficulty of observing the crystal growth in real time, and the chemical bath deposition takes hours to complete and is not able to produce mono- or few-layered Bi_2O_2S nanosheets. Hence there is a need for a simple yet cost-effective method for producing a thermodynamically stable suspension of Bi_2O_2S nanosheets under ambient conditions. In this study, Bi_2O_2S nanosheets were synthesized at room temperature *via* a one-pot wet-chemical synthetic method. Specifically, bismuth nitrate or $Bi(NO_3)_3$ was used as the Bi source, and thiourea (CH_4N_2) was chosen as the S source. The reaction was conducted under basic conditions in the presence of hydrazine. The low-cost room-temperature synthesis of free-standing Bi_2O_2S nanosheets with high yield can be readily employed for large-area device applications, which is independent of the substrate in comparison with nanosheets grown over substrates.

Experimental

100 mg (0.206 mmol) of $Bi(NO_3)_3{\cdot}5H_2O$, 7.84 mg (0.103 mmol) of CH_4N_2S, 1 ml of hydrazine hydrate and 306.8 mg (0.824 mmol) of disodium EDTA were used as the starting chemicals. 100 mg (0.206 mmol) of $Bi(NO_3)_3{\cdot}5H_2O$ was dissolved in 20 ml of water by sonication, producing a transparent solution. 1 ml of hydrazine hydrate was added to a separate vial containing CH_4N_2S (12.7 mg). Finally, 120 mg of KOH and 320 mg of NaOH were added into the solution and were left overnight to obtain brown color precipitates. The product was then washed with water and dried in a desiccator overnight. The X-ray diffraction data were collected using a Panalytical X'Pert PRO MRD HR XRD System. HORIBA LabRAM Evolution RAMAN Microscope-Smart SPM atomic force microscope was used to obtain Raman spectra of Bi_2O_2S samples with a 633 nm laser. Also, the AFM image was obtained using the same instrument. The UV-Vis-NIR absorption spectrum of the synthesized nanosheets were obtained by employing a UV 3000 spectrophotometer. Scanning electron microscopy (SEM) and transmission electron microscopy (TEM) studies were performed using an FEI Verios 460L SEM, and an FEI Tecnai T12 G2 TWIN TEM operating at 120 kV. The photodetection device was fabricated by thermally evaporating Ti (5 nm)/Au (200 nm) over pre-cleaned Si/SiO_2 with 285 nm of oxide layer using a shadow mask. The distance between the two electrodes was around 10 μm with ~1.3 mm width. Bi_2O_2S nanosheets dispersed in water (3 mg ml^{-1}) using sonication, were drop-cast over the electrodes and dried overnight in a vacuum. The thickness of the Bi_2O_2S nanosheet film was around 1 μm as measured using a Dektak 150 stylus profilometer (Fig. S1, ESI†) and AFM (Fig. S2, ESI†). The current–voltage characteristics of the device were measured using a Keysight B2902A Precision Source/Measure Unit. A HORIBA LabRAM Evolution RAMAN Microscope-Smart SPM atomic force microscope equipped with 532 nm, 633 nm and 785 nm laser was used as the light source in the present study. The intensity of the laser was calculated using a calibrated Si photodiode. The difference between the current under illumination and in the dark corresponds to the photocurrent.

Results and discussion

The scalable room-temperature synthesis of Bi_2O_2S nanosheets was carried out by reacting $Bi(NO_3)_3$ in water and thiourea in hydrazine hydrate, respectively. Eqn (1) and (2) show the chemical reactions involved in the formation of Bi_2O_2S nanosheets. In the first step, $Bi(NO_3)_3$ undergoes hydrolysis to produce $BiONO_3$ and the hydrolysis process is expedited in alkaline medium. In the second step, S^{2-} resulting from the decomposition of thiourea interacts with $BiONO_3$ to form Bi_2O_2S, and the self-assembly of oppositely charged $(Bi_2O_2)^{2+}$ and S^{2-} layers results in the formation of ultrathin Bi_2O_2S nanosheets, which are precipitated as a dark brown color product in the aqueous medium.

$$Bi(NO_3)_3 + H_2O \rightarrow BiONO_3 + 2H^+ + 2NO_3^- \quad (1)$$

$$2BiONO_3 + SC(NH_2)_2 + 2OH^- \rightarrow Bi_2O_2S + OC(NH_2)_2 + 2NO_3^- + H_2O \quad (2)$$

Fig. 1a illustrates the crystal structure of Bi_2O_2S having alternating stacks of $[Bi_2O_2]_n^{2n+}$ and S_n^{2n-} layers, manifesting as weak interlayer interactions.[39] Fig. 1b shows the typical XRD pattern of vacuum-dried Bi_2O_2S nanosheets[31] corresponding to the orthorhombic *Pnnm* space group (JCPDS no. 34-1493). Vacuum drying of Bi_2O_2S nanosheets leads to the agglomeration of the nanosheets giving rise to clear peaks in the XRD pattern.[40] Fig. 1c shows the Raman spectrum of ultrathin Bi_2O_2S nanosheets acquired using a 633 nm laser showing theoretically predicted Raman peaks at around 164 cm^{-1} (A_g mode) and 263 cm^{-1} (B_{1g} mode).[41] The broad hump around 217 cm^{-1} is due to the underlying Si/SiO_2 substrate. The UV-Vis-NIR absorption spectrum of Bi_2O_2S nanosheets is shown in Fig. 1d. The spectrum exhibits an absorption edge near 1000 nm, corresponding to an intrinsic bandgap absorption edge around 1.5 eV, which is in excellent agreement with what has been previously reported in the literature.[31,33,34]

In Fig. 2a, we show a TEM image of Bi_2O_2S nanosheets confirming the nanosheet morphology as crumpled nanosheets due to the weak electrostatic interaction between the layers. The AFM image of the Bi_2O_2S nanosheets with the corres-

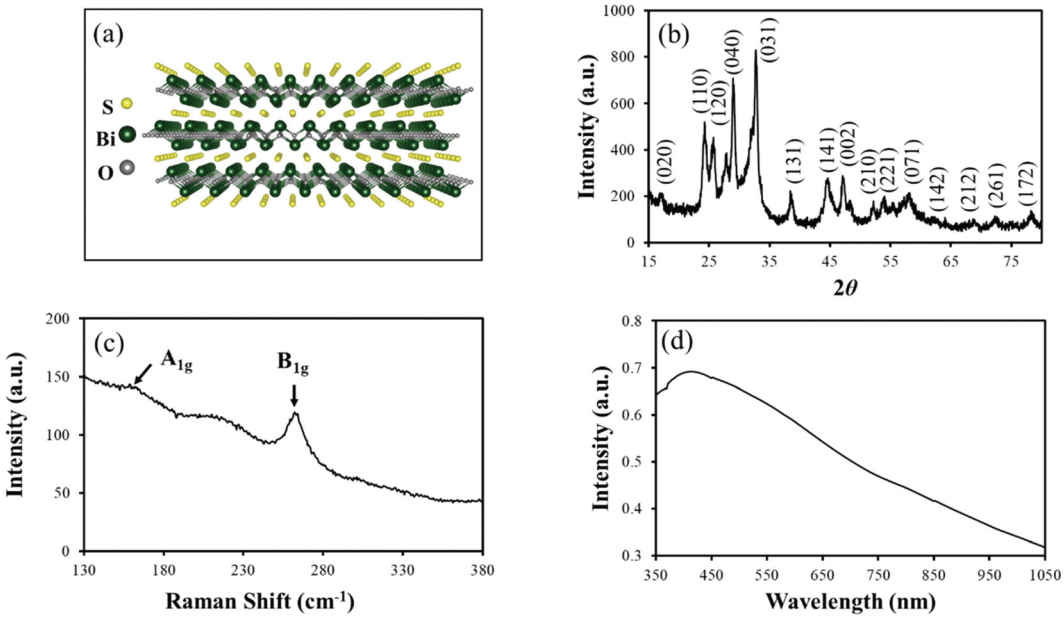

Fig. 1 (a) Crystal structure of Bi_2O_2S.[38] (b) XRD pattern of vacuum dried Bi_2O_2S nanosheets. (c) Raman spectrum of Bi_2O_2S nanosheets. (d) UV-VIS-NIR absorption spectrum of Bi_2O_2S nanosheets.

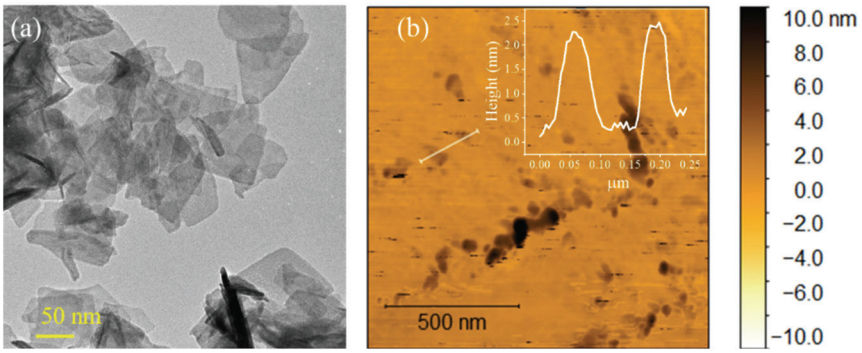

Fig. 2 (a) TEM image of Bi_2O_2S nanosheets. Scale bar: 50 nm. (b) AFM image of Bi_2O_2S nanosheets with the corresponding height profile as inset. Scale bar: 500 nm.

ponding height profile (inset) is shown in Fig. 2b. The lateral dimension of the Bi_2O_2S nanosheets was around 80–200 nm with a thickness of ~2–3 nm corresponding to 2–3 layers, thus confirming the ultrathin nature of Bi_2O_2S nanosheets.

To further demonstrate the feasibility of solution-processed ultrathin Bi_2O_2S nanosheets for photodetection, we fabricated a two-terminal NIR photodetection device by drop-casting, as shown in Fig. 3a. We examined the current–voltage (*I–V*) characteristics of the device in the dark and under 785 nm with varying light intensity. As illustrated in Fig. 3b, the linear *I–V* indicates the ohmic contact between electrodes and Bi_2O_2S nanosheets. The mechanism behind the photodetection is presented as the inset in Fig. 3b. Upon illuminating the device with a NIR light source, the absorption of the NIR light generates electron–hole pairs,[3,22,42] which in turn can be extracted on applying bias voltage across the device. The photoresponse in a photoconductor comprises of photoconductive response (fast response at low intensity) and bolometric response (slow response at high intensity).[27] We have considered the photoconductive response to be the major contributor which is evident from the fast variation of photocurrent *vs.* illumination intensity. Fig. 3c depicts the current *vs.* time response of the device with different intensities at 785 nm. The photocurrent was measured at 5 V with the NIR source being switched on and off, showing the reproducibility as well as transient response. The variation of photocurrent *vs.* illumination intensity shows that the electrical conductivity of the device increases with increasing light intensity due to the absorption of more photons resulting in a larger photocurrent. To confirm the selectivity of the photodetectors, we have tested the device under 785 nm, 633 nm and 532 nm illumination with 40 mW cm^{-2} (Fig. 3d). We can clearly see from Fig. 3d

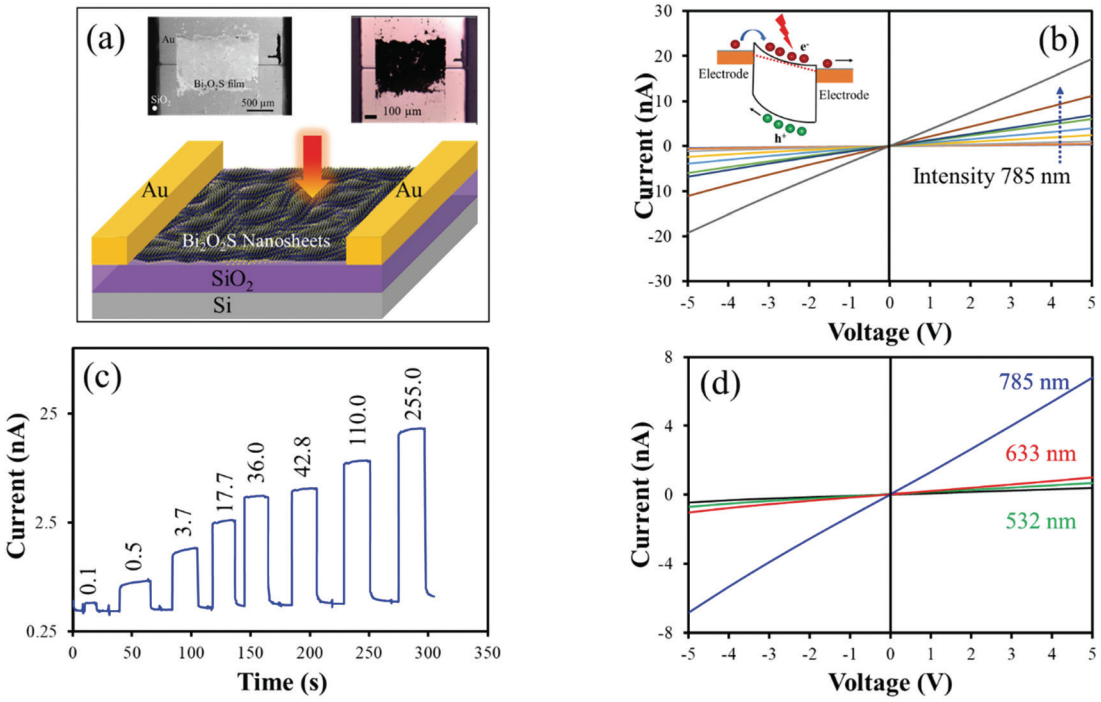

Fig. 3 (a) Schematic of the photodetection device. Inset: SEM image of the device (left) and optical image of the device (right). (b) *I*–*V* characteristics of the Bi_2O_2S nanosheet device in the dark and under different illumination intensities at 785 nm. The inset shows the mechanism behind the detection. (c) Transient photoresponse of the device under different illumination of 785 nm at 5 V. The values in the inset represent the intensity in mW cm^{-2}. (d) *I*–*V* characteristics of the device under darkness, 532 nm, 633 nm and 785 nm with the light intensity of 40 mW cm^{-2}.

that the photoresponse is dependent on the wavelength of the illumination source. This could be attributed to the fact that the bandgap of the Bi_2O_2S nanosheets is around 1.5 eV, *i.e.* closer to 785 nm rather than 633 nm and 532 nm.

The applicability of these solution-processed photodetection devices demands their photoresponsivity and external quantum efficiency to be high, the two important parameters for commercial photodetector applications.[3,43,44] The photoresponsivity is defined corresponding to the photocurrent generated per unit power of the incident light and the external quantum efficiency (EQE), *i.e.* the number of electrons detected per incident photon can be calculated as $R_\lambda = I_\lambda/P_\lambda S$, EQE = $hcR_\lambda/e\lambda$ respectively, where I_λ corresponds to the photocurrent ($I_{light} - I_{dark}$), P_λ the intensity of light, S the device effective area under illumination, h Planck's constant, e the electronic charge, c the velocity of the light, and λ the illumination wavelength. The normalized photocurrent-to-dark-current ratio (NPDR)[45,46] derived from the ratio of the responsivity to the dark current, was also calculated for the device.

The photoresponsivity of the devices decreases with increasing intensity as the responsivity is inversely proportional to the laser intensity (Fig. 4a).[47] The inset in Fig. 4a corresponds to increased photocurrent *vs.* illumination intensity as explained earlier. Another parameter deciding the applicability of the photodetection device in practical application is the response and recovery time of the photodetector (Fig. 4b). The time constants for photocurrent growth and decay can be estimated by the equations $I(t) = I_{dark} + A[1 - \exp(-(t - t_0)/\tau_1)] + B[1 - \exp(-(t - t_0)/\tau_2)]$ and $I(t) = I_{dark} + A[\exp(-(t - t_0)/\tau_1)] + B[\exp(-(t - t_0)/\tau_2)]$ respectively, where I_{dark} is the dark current, τ is the time constant, t_0 corresponds to IR switch on and off time, and A and B are scaling constants. In Fig. 4b, the red line shows the fitting over experimental data (open circles). The photocurrent rises rapidly in 100 ms followed by a slower component where the photocurrent takes nearly 11 s before saturation. During photocurrent decay, the current drops quickly within 160 ms, further taking 488 ms to reach its initial value. Our device exhibited a photoresponsivity of 4 A W^{-1}, an EQE of 630% and an NPDR of 1.3×10^{10} per watt. We have compared the photodetection performance of our device with other 2D materials as depicted in Table 1.

As evident from Table 1, the photodetection performance of our Bi_2O_2S nanosheet photodetector is comparable to those fabricated from graphene,[48] black phosphorus,[50] GaSe,[42] $MoTe_2$,[13] Bi_2S_3,[51] and Bi_2Se_3 [52] and lower than that of MoS_2 [53] and Bi_2O_2Se.[28,43] The biggest advantage of our approach is the room-temperature synthesis method in comparison with CVD growth or high temperature methods to obtain crystals needed for exfoliation. In the present study, the room-temperature growth offers low cost and the possibility of fabrication of large area devices. The device showed excellent stability even after exposure to air for a month indicating the air stability of Bi_2O_2S nanosheets.

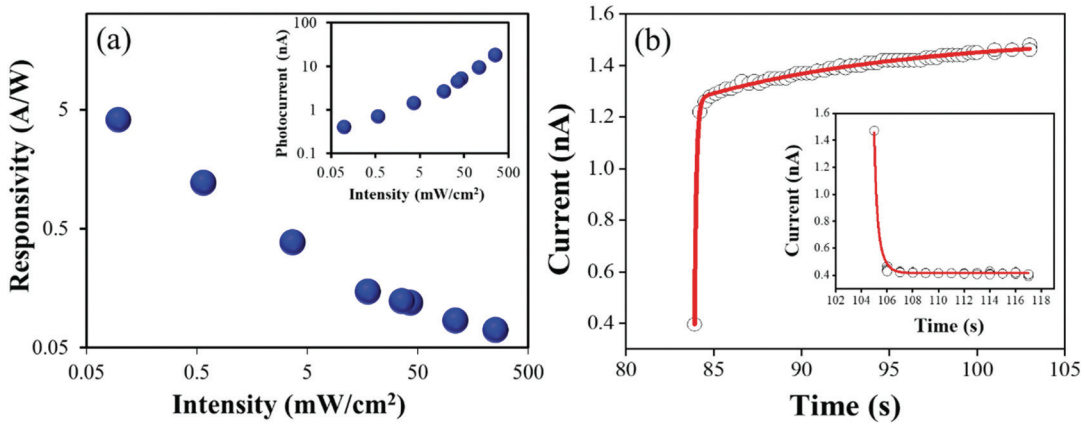

Fig. 4 (a) Photoresponsivity *vs.* intensity with the photocurrent as a function of light intensity shown as the inset. (b) Transient time response of photocurrent growth and decay (inset) for the Bi_2O_2S nanosheet photodetector. The open circles are the experimental data points and the solid lines are a fit to the equation.

Table 1 Performance of 2D material-based photodetectors

2D material	Synthesis technique	Responsivity (A W^{-1})	Response time (ms)	Detection range	NPDR (W)	Ref.
Graphene	Exfoliation	6×10^{-3}	6×10^{-8}	UV-SWIR	—	48
MoS_2	Exfoliation	2570	2	Visible	2.5×10^{14}	49
Black P	Exfoliation	1.5	0.02	NIR	7.5×10^{6}	50
GaSe	Exfoliation	2.8	20	UV	2.3×10^{9}	42
$MoTe_2$	Exfoliation	6	0.1	NIR	3.0×10^{8}	13
Bi_2O_2Se	CVD	2000	—	Visible	7.0×10^{11}	28
Bi_2O_2Se	CVD	3.5×10^{4}	0.30	Visible	3.5×10^{10}	43
Bi_2S_3	Solvothermal	4.4	0.01	Vis-NIR	2.2×10^{7}	51
Bi_2Se_3	CVD	23.8	540	NIR	2.4×10^{9}	52
Bi_2O_2S	RT wet chemical	4	100	NIR	1.3×10^{10}	This work

It is worth noting that the present investigation shows the measurement performed on a single device. However, the goal of this study is to highlight the new room-temperature synthesis method for obtaining Bi_2O_2S nanosheets. Photodetection has already been demonstrated in hydrothermally grown Bi_2O_2S.[32,35] It is anticipated that there will be small variation in device performance associated with the drop-casting method owing to varied nanosheet density and thickness of the film. Further optimization of the reproducibility or photoresponsivity can be accomplished by other thin-film deposition techniques such as spin coating, spray coating, inkjet printing *etc.*[54,55]

Conclusions

To summarize, we demonstrate for the first time, a facile synthesis of freestanding Bi_2O_2S nanosheets under ambient conditions. The nanosheets were ultrathin with a thickness of around 2–3 nm. The synthesis method produces high yield air-stable nanosheets. Under 785 nm laser illumination, the solution-processed photodetector based on Bi_2O_2S nanosheets showed high performance with a photoresponsivity of 4 A W^{-1}, an external quantum efficiency of 630%, and an NPDR of 1.3×10^{10} per watt. Therefore, this study puts forward air stable Bi_2O_2S nanosheets in conjugation with other 2D materials for exploitation in future large area flexible optoelectronics.

Conflicts of interest

There are no conflicts to declare.

Acknowledgements

The authors are grateful for the financial support of this project by the U.S. National Science Foundation (Awards # 1831133 and #1523617). This work was performed in part at the Duke University Shared Materials Instrumentation Facility (SMIF), and at the Analytical Instrumentation Facility (AIF) at North Carolina State University. Both facilities are members of the North Carolina Research Triangle Nanotechnology Network (RTNN), which is supported by the National Science Foundation (Grant ECCS-1542015) as part of the National Nanotechnology Coordinated Infrastructure (NNCI). The authors thank Michelle Plue, Talmage Tyler, Kirk Bryson, Fred Stevie, and Phillip Strader for their excellent technical assistance.

References

1 C.-H. Liu, Y.-C. Chang, T. B. Norris and Z. Zhong, *Nat. Nanotechnol.*, 2014, **9**, 273–278.
2 F. Wang, Y. Zhang, Y. Gao, P. Luo, J. Su, W. Han, K. Liu, H. Li and T. Zhai, *Small*, 2019, **15**, 1901347.
3 Z. Yin, H. Li, H. Li, L. Jiang, Y. Shi, Y. Sun, G. Lu, Q. Zhang, X. Chen and H. Zhang, *ACS Nano*, 2012, **6**, 74–80.
4 M. W. Geis, S. J. Spector, M. E. Grein, J. U. Yoon, D. M. Lennon and T. M. Lyszczarz, *Opt. Express*, 2009, **17**, 5193–5204.
5 H. H. Tseng, H. Li, V. Mashanov, Y. J. Yang, H. H. Cheng, G. E. Chang, R. A. Soref and G. Sun, *Appl. Phys. Lett.*, 2013, **103**, 231907.
6 N. Huo and G. Konstantatos, *Adv. Mater.*, 2018, **30**, 1801164.
7 K. S. Novoselov, A. K. Geim, S. V. Morozov, D. Jiang, Y. Zhang, S. V. Dubonos, I. V. Grigorieva and A. A. Firsov, *Science*, 2004, **306**, 666–669.
8 D. J. Late, B. Liu, H. S. S. Ramakrishna Matte, V. P. Dravid and C. N. R. Rao, *ACS Nano*, 2012, **6**, 5635–5641.
9 D. J. Late, Y.-K. Huang, B. Liu, J. Acharya, S. N. Shirodkar, J. Luo, A. Yan, D. Charles, U. V. Waghmare, V. P. Dravid and C. N. R. Rao, *ACS Nano*, 2013, **7**, 4879–4891.
10 C. Lee, X. Wei, J. W. Kysar and J. Hone, *Science*, 2008, **321**, 385–388.
11 B. Chitara and A. Ya'akobovitz, *Nanoscale*, 2018, **10**, 13022–13027.
12 K. Liu, Q. Yan, M. Chen, W. Fan, Y. Sun, J. Suh, D. Fu, S. Lee, J. Zhou, S. Tongay, J. Ji, J. B. Neaton and J. Wu, *Nano Lett.*, 2014, **14**, 5097–5103.
13 T. J. Octon, V. K. Nagareddy, S. Russo, M. F. Craciun and C. D. Wright, *Adv. Opt. Mater.*, 2016, **4**, 1750–1754.
14 X. Chen, X. Lu, B. Deng, O. Sinai, Y. Shao, C. Li, S. Yuan, V. Tran, K. Watanabe, T. Taniguchi, D. Naveh, L. Yang and F. Xia, *Nat. Commun.*, 2017, **8**, 1–7.
15 X. Wang, W. Tian, M. Liao, Y. Bando and D. Golberg, *Chem. Soc. Rev.*, 2014, **43**, 1400–1422.
16 X. Yu, S. Zhang, H. Zeng and Q. J. Wang, *Nano Energy*, 2016, **25**, 34–41.
17 F. Luo, M. Zhu, Y. Tan, H. Sun, W. Luo, G. Peng, Z. Zhu, X.-A. Zhang and S. Qin, *AIP Adv.*, 2018, **8**, 115106.
18 Q. Li, Q. Zhou, L. Shi, Q. Chen and J. Wang, *J. Mater. Chem. A*, 2019, **7**, 4291–4312.
19 L. Zhang, S. Shen, M. Li, L. Li, J. Zhang, L. Fan, F. Cheng, C. Li, M. Zhu, Z. Kang, J. Su, T. Zhai and Y. Gao, *Adv. Opt. Mater.*, 2019, **7**, 1801744.
20 T. Limbu, B. Chitara, J. D. Orlando, M. G. Cervantes, S. Kumari, Q. Li, Y. Tang and F. Yan, *J. Mater. Chem. C*, 2020, **8**, 4722–4731.
21 J. Wu, H. Yuan, M. Meng, C. Chen, Y. Sun, Z. Chen, W. Dang, C. Tan, Y. Liu, J. Yin, Y. Zhou, S. Huang, H. Q. Xu, Y. Cui, H. Y. Hwang, Z. Liu, Y. Chen, B. Yan and H. Peng, *Nat. Nanotechnol.*, 2017, **12**, 530–534.
22 J. Li, Z. Wang, Y. Wen, J. Chu, L. Yin, R. Cheng, L. Lei, P. He, C. Jiang, L. Feng and J. He, *Adv. Funct. Mater.*, 2018, **28**, 1706437.
23 Q. Wei, R. Li, C. Lin, A. Han, A. Nie, Y. Li, L.-J. Li, Y. Cheng and W. Huang, *ACS Nano*, 2019, **13**, 13439–13444.
24 H. Yang, W. Chen, X. Zheng, D. Yang, Y. Hu, X. Zhang, X. Ye, Y. Zhang, T. Jiang, G. Peng, X. Zhang, R. Zhang, C. Deng and S. Qin, *Nanoscale Res. Lett.*, 2019, **14**, 371.
25 C. Tan, M. Tang, J. Wu, Y. Liu, T. Li, Y. Liang, B. Deng, Z. Tan, T. Tu, Y. Zhang, C. Liu, J.-H. Chen, Y. Wang and H. Peng, *Nano Lett.*, 2019, **19**, 2148–2153.
26 J. Wu, C. Qiu, H. Fu, S. Chen, C. Zhang, Z. Dou, C. Tan, T. Tu, T. Li, Y. Zhang, Z. Zhang, L.-M. Peng, P. Gao, B. Yan and H. Peng, *Nano Lett.*, 2019, **19**, 197–202.
27 H. Yang, C. Tan, C. Deng, R. Zhang, X. Zheng, X. Zhang, Y. Hu, X. Guo, G. Wang, T. Jiang, Y. Zhang, G. Peng, H. Peng, X. Zhang and S. Qin, *Small*, 2019, **15**, e1904482.
28 J. Wu, Y. Liu, Z. Tan, C. Tan, J. Yin, T. Li, T. Tu and H. Peng, *Adv. Mater.*, 2017, **29**, 1704060.
29 J. Li, Z. Wang, J. Chu, Z. Cheng, P. He, J. Wang, L. Yin, R. Cheng, N. Li, Y. Wen and J. He, *Appl. Phys. Lett.*, 2019, **114**, 151104.
30 E. P. Painter, *Chem. Rev.*, 1941, **28**, 179–213.
31 X. Zhang, Y. Liu, G. Zhang, Y. Wang, H. Zhang and F. Huang, *ACS Appl. Mater. Interfaces*, 2015, **7**, 4442–4448.
32 Z. Wu, H. Yu, S. Shi and Y. Li, *J. Mater. Chem. A*, 2019, **7**, 14776–14789.
33 A. L. Pacquette, H. Hagiwara, T. Ishihara and A. A. Gewirth, *J. Photochem. Photobiol., A*, 2014, **277**, 27–36.
34 C. Huang, H. Yu, J. Chen, J. Zhang, Z. Wu and C. Hou, *Sol. Energy Mater. Sol. Cells*, 2019, **200**, 110030.
35 E. A. Bondarenko, E. A. Streltsov, M. V. Malashchonak, A. V. Mazanik, A. I. Kulak and E. V. Skorb, *Adv. Mater.*, 2017, **29**, 1702387.
36 E. A. Bondarenko, E. A. Streltsov, A. V. Mazanik and A. I. Kulak, *ChemElectroChem*, 2019, **6**, 2474–2481.
37 M. Wu and X. C. Zeng, *Nano Lett.*, 2017, **17**, 6309–6314.
38 K. Momma and F. Izumi, *J. Appl. Crystallogr.*, 2008, **41**, 653–658.
39 A. Jain, S. P. Ong, G. Hautier, W. Chen, W. D. Richards, S. Dacek, S. Cholia, D. Gunter, D. Skinner, G. Ceder and K. A. Persson, *APL Mater.*, 2013, **1**, 011002.
40 T. Ghosh, M. Samanta, A. Vasdev, K. Dolui, J. Ghatak, T. Das, G. Sheet and K. Biswas, *Nano Lett.*, 2019, **19**, 5703–5709.
41 T. Cheng, C. Tan, S. Zhang, T. Tu, H. Peng and Z. Liu, *J. Phys. Chem. C*, 2018, **122**, 19970–19980.
42 P. Hu, Z. Wen, L. Wang, P. Tan and K. Xiao, *ACS Nano*, 2012, **6**, 5988–5994.
43 Q. Fu, C. Zhu, X. Zhao, X. Wang, A. Chaturvedi, C. Zhu, X. Wang, Q. Zeng, J. Zhou, F. Liu, B. K. Tay, H. Zhang, S. J. Pennycook and Z. Liu, *Adv. Mater.*, 2019, **31**, 1804945.
44 P. Luo, F. Zhuge, F. Wang, L. Lian, K. Liu, J. Zhang and T. Zhai, *ACS Nano*, 2019, **13**, 9028–9037.
45 C. On Chui, A. K. Okyay and K. C. Saraswat, *IEEE Photonics Technol. Lett.*, 2003, **15**, 1585–1587.
46 N. Youngblood, C. Chen, S. J. Koester and M. Li, *Nat. Photonics*, 2015, **9**, 247–252.

47 T.-F. Zhang, Z.-P. Li, J.-Z. Wang, W.-Y. Kong, G.-A. Wu, Y.-Z. Zheng, Y.-W. Zhao, E.-X. Yao, N.-X. Zhuang and L.-B. Luo, *Sci. Rep.*, 2016, **6**, 1–8.
48 T. Mueller, F. Xia and P. Avouris, *Nat. Photonics*, 2010, **4**, 297–301.
49 X. Wang, P. Wang, J. Wang, W. Hu, X. Zhou, N. Guo, H. Huang, S. Sun, H. Shen, T. Lin, M. Tang, L. Liao, A. Jiang, J. Sun, X. Meng, X. Chen, W. Lu and J. Chu, *Adv. Mater.*, 2015, **27**, 6575–6581.
50 F. Gong, F. Wu, M. Long, F. Chen, M. Su, Z. Yang and J. Shi, *Phys. Status Solidi RRL*, 2018, **12**, 1800310.
51 G. Chen, Y. Yu, K. Zheng, T. Ding, W. Wang, Y. Jiang and Q. Yang, *Small*, 2015, **11**, 2848–2855.
52 F. Wang, L. Li, W. Huang, L. Li, B. Jin, H. Li and T. Zhai, *Adv. Funct. Mater.*, 2018, **28**, 1802707.
53 O. Lopez-Sanchez, D. Lembke, M. Kayci, A. Radenovic and A. Kis, *Nat. Nanotechnol.*, 2013, **8**, 497–501.
54 F. P. García de Arquer, A. Armin, P. Meredith and E. H. Sargent, *Nat. Rev. Mater.*, 2017, **2**, 1–17.
55 R. Swartwout, M. T. Hoerantner and V. Bulović, *Energy Environ. Mater.*, 2019, **2**, 119–145.